3D-PTV Measurements of an Axisymmetric Synthetic Jet

Kamal Raj Sharma, Malkeet Singh, Jyoti Gupta, and Arun K. Saha

Abstract The present study aims to measure the volumetric flow field of a circular synthetic jet using three-dimensional particle tracking velocimetry (3D-PTV). The statistical flow characteristics of the synthetic jet have been discussed using ensemble-averaged velocities and their fluctuations. The 3D-PTV data is compared with the 2D-PIV data for the same formation number. The jet width is different in both cases, which owes to the difference in the orifice configuration in the two measurement cases. The streamwise velocity and root mean square velocity dominates the flow owing to the induced velocity of the vortex rings. The transverse velocity and its fluctuations are more than the vertical velocity and its fluctuation. The time evolution of the circular vortex ring has also been shown for two actuation cycles using isosurfaces plots of the normalized vorticity magnitude, which infers that the induced velocity of the vortex ring remains nearly the same throughout the flow field. The streamwise turbulence decreases along the downstream direction, but the ring loses its coherence in the far field due to persisting vertical and transverse turbulence.

Keywords Synthetic jet · Vortex ring · Three-dimensional particle tracking velocimetry (3D-PTV) · Ensemble average · Vorticity magnitude

Nomenclature

υ	Kinematic viscosity of water [m^2/s]
U_o	Average blowing velocity [m/s]
f_a	Actuation frequency [Hz]
T	The time of an actuation cycle s
L	Formation number –
f	Acquisition frequency [Hz]

K. R. Sharma (✉) · M. Singh · J. Gupta · A. K. Saha
Department of Mechanical Engineering, IIT Kanpur, Kanpur 208016, India
e-mail: ksharma1@me.iitr.ac.in

D	Diameter of the synthetic jet orifice [mm]
U, V, W	Streamwise, vertical, and transverse velocity [m/s]
$U_{\mathrm{rms}}, V_{\mathrm{rms}}, W_{\mathrm{rms}}$	Root mean square streamwise, vertical, and transverse velocities [m/s]
$\overline{\omega}, \omega$	Ensemble-averaged and instantaneous vorticity magnitude [1/s]
$\omega/\omega_{\mathrm{max}}$	Normalized instantaneous vorticity magnitude –
Q/Q_{max}	Normalized Q-criteria –

1 Introduction

The synthetic jet produces a train of vortex rings, a complex three-dimensional flow with many engineering applications like modifications of bluff body aerodynamics, control of lift and drag of airfoils, reduction of skin friction in planar boundary layers, and heat transfer enhancement [1–4]. A synthetic jet is produced by an alternating fluid suction and ejection from an orifice maintaining a zero net mass flux but transferring linear momentum to the surrounding fluid. The jet is formed entirely from the fluid in which it is employed. Hence, the actuator can be integrated into the flow surface without needing extra fluid supply, making it feasible for external and internal flow control. The synthetic jet actuator contains an orifice on one side and a diaphragm on the other side of a cavity. There are a few performance factors of the actuator based on the given application, like maximum jet velocity, jet spreading rate, and mass flow rate.

A flow starts to form around the orifice edge when the diaphragm starts to move. The initially thin boundary layer separates at the nozzle edge, causing a vortex to spiral up and forms a closed vortical structure called vortex ring by entraining surrounding irrotational fluid. As the diaphragm stops pushing the fluid the induced velocity of the vortex ring advects the ring downstream. The synthetic jet flow is dominated by three regions [5], first is the near field which is dominated by the formation and advection of the time-periodic vortex rings. Characteristic length scale and celerity of the discrete vortex rings depend upon the orifice size, amplitude, and period of the diaphragm motion. The impulse the diaphragm provides to the vortex ring should be larger than the suction and frictional forces. The second region is a transitional region in which the vortex rings entrain the ambient fluid, and the third is a far-field region in which the vortex rings slow down, lose coherence as they break down into smaller vortical structures, and eventually, the flow becomes turbulent.

2   Literature Review and Objective

Many studies have revealed the flow structure of the circular synthetic jet both exper-
imentally and numerically. It has been shown that the axisymmetric synthetic jet
development and evolution of vortex rings are mainly affected by two primary dimen-
sionless numbers, namely stroke length and Reynolds number [6], as shown in Eqs. 1
and 2, respectively, where U_o is the time-averaged expulsion velocity over one actua-
tion cycle, shown in Eq. 3. At the same time, the Stokes number and Strouhal number
determine the formation criteria of the synthetic jet, shown in Eqs. 4, 5, and 6. K is
the jet formation constant of 0.16 for axisymmetric synthetic jets [7].

$$L = \frac{L_o}{D} = U_o/f_a D \tag{1}$$

$$\mathrm{Re} = U_o D/\upsilon \tag{2}$$

$$U_o = \frac{1}{T} \int_0^{T/2} u(t)\mathrm{d}t \tag{3}$$

$$St_K = D\sqrt{\frac{f_a}{\upsilon}} \tag{4}$$

$$St = \frac{f_a D}{U_o} \tag{5}$$

$$\frac{1}{St} = \frac{\mathrm{Re}}{St_k^2} > K \tag{6}$$

Apart from the actuation and fluid parameters, the effect of geometrical parameters
on the performance of the synthetic jet has also been studied in the literature. The
effect of orifice shape, edge configurations, orifice depth, and cavity size significantly
impacts the evolution of the vortex rings. The higher aspect ratio of the orifice gives
rise to the phenomenon of axis-switching and bifurcation [8, 9]. The other geometric
parameters also affect the maximum jet exit velocity [10].

Among the experimental methods used in the literature to characterize the flow
phenomenon of the synthetic jet, planar particle image velocimetry (2D-PIV) has
been extensively used. The planar-PIV measuring technique offers several benefits,
like non-intrusive flow field measurement in an instant, but it has also been noted
in the literature that it overestimates a few turbulent flow properties [11]. Addi-
tionally, the light sheet illumination determines the particle's out-of-plane location
in both classic planar and stereoscopic PIV approaches. Since a volumetric flow
measurement technique illuminates the volume so the depth position of the particle
cannot be assumed. Three-dimensional flow structures of the synthetic jet have been

reported using stereoscopic PIV in the literature recently [12, 13]. The evolution of circular and non-circular vortex rings has been shown in these studies. Volumetric studies on the flow problem are very rare. 3D-PTV offers more accuracy and spatial resolution than cross-correlation-based volumetric flow measuring techniques like tomographic PIV [14]. The present study enriches the experimental database with the 3D-PTV measurement of a circular synthetic jet showing various three-dimensional flow parameters.

2.1   Materials and Methods

The present study was conducted in the water tunnel facility in the Department of Mechanical Engineering, IIT Kanpur. The synthetic jet was installed in a rectangular quiescent water tank of $1000 \times 500 \times 500$ mm. The cavity of the synthetic jet, having an inner diameter of 70 mm, was fixed at the center of one side of the tank, as shown in Fig. 1. The diaphragm was attached to one side of the cavity, and the orifice plate was on the other. The diaphragm was actuated with a cam-follower arrangement powered by a brushless DC motor. The orifice plate has an outer diameter of 90 mm and a thickness of 2 mm. The orifice was extended up to the nearest possible field of view of the cameras by a nozzle of 70 mm and inner diameter, $D = 8$ mm. The Reynolds number based on U_o (average blowing velocity per actuation cycle) and D was kept at 1075. All the non-dimensional numbers related to the study are shown in Eqs. 1–6, and their concerned values in the study are shown in Table 1. The non-dimensional numbers used in the study ensure the proper vortex roll-up as the value of $Re/St_k{}^2$ (Eq. 6) in the present study is higher than the jet formation constant for the axisymmetric jet case. The actuation frequency (f_a) of the synthetic jet was kept at 5.6 Hz.

The 3D-PTV experimental setup consisted of three Phantom VEO 340 L cameras (2560×1600 pixels) fitted with 135 mm Zeiss lenses. The cameras were arranged in a linear array, as shown in Fig. 1, and focused on the measurement volume with a nominal magnification of 0.44. The capture rate was kept at 25 Hz. The cameras were positioned using a 2D traverse system (ISEL, Germany) to capture the field of view with half resolution (1280×800 pixels). Polyamide tracer particles were used with a mean diameter of 50 μm. A dual head Nd: YLF laser (Photonics DM-50-527DH) was used as the illumination source, which passed through a light arm and a series of light sheet optics that created illumination volume.

The final measurement volume of the overlapped cameras was $60 \times 40 \times 40$ mm. The laser and cameras were synchronized with a synchronizer (610036) with a timing precision of 250 ns. The calibration was performed by traversing a single plane calibration target using a 1D traverse at 21 different positions spaced 2 mm apart in the depth of the measuring volume. The mapping functions for projections and back projections were obtained. The calibration image processing and 3D-PTV were accomplished using INSIGHT V3V-4G software. The two independent image frames were separated by a short time interval ('Δt') equal to 3000 μs in the present study.
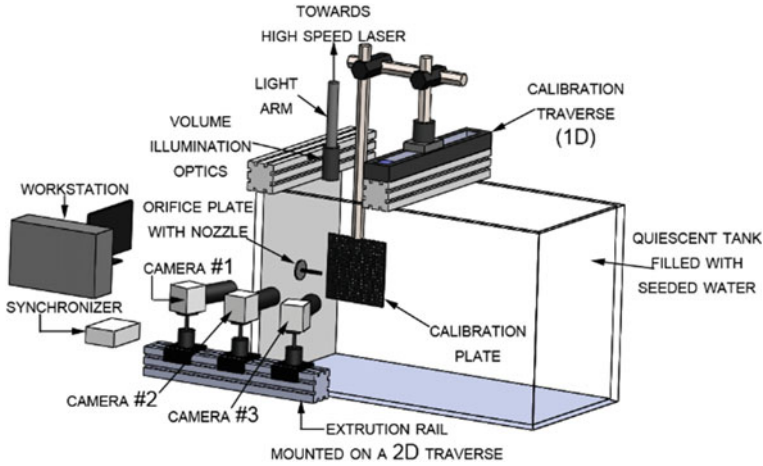
Fig. 1 Schematic of the experimental setup

Table 1 Important flow parameters of the study

Important parameters	Value
Formation number (L)	2.73
Characteristic velocity (U_o in m/s)	0.12
Reynolds number (Re, based on U_o and D)	1075
Stokes number (St_k)	19.84
Strouhal number (St)	0.37

The ensemble-averaged 3D vectors were obtained using 50 instantaneous fields. A total of $30 \times 20 \times 19$ vectors were obtained in the X, Y, and Z directions after velocity interpolation with 50% overlap, giving the spatial resolution of 2 mm. The projection error of less than 1 pixel was observed from calibration for all three apertures, along with a mean dewarping error of fewer than 20 μm.

Figure 2a shows the evolution of all three non-dimensional velocity components over the experimental time. Nearly ten cycles of the synthetic jet were captured. The streamwise velocity (U) plot shows the periodic behavior occurring at the actuation frequency of the synthetic jet actuator ($f_a = 5.6$ Hz), as shown in the FFT of the streamwise velocity (U) in Fig. 2b. The vertical (V) and transverse (W) velocity components show marginal fluctuations.
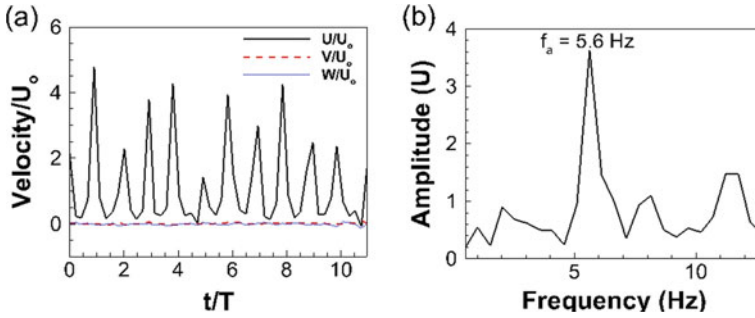
Fig. 2 **a** Temporal evolution of non-dimensional velocity components (U, V, and W) obtained near the jet orifice at $X/D = 1.25$, $Y/D = Z/D = 0$ and **b** FFT of the streamwise velocity (U)

3   Results and Discussion

3.1   Ensemble-Averaged Flow Field

The present section shows the ensemble-averaged 3D vector field of an axisymmetric synthetic jet with $L = 2.73$ and Re = 1075 for 50 instantaneous flow fields obtained using 3D-PTV. The origin ($X/D = Y/D = Z/D = 0$) of the 3D vector flow field is taken at the nozzle orifice. The comparison of the 2D-PIV and 3D-PTV data for the nearly same formation number but two different Reynolds numbers has been shown in Fig. 3. The data obtained from the two measurement techniques have been compared for two streamwise locations, $X.D = 2$ and 6. It can be seen from the figure that the velocity profiles do not agree as far as the jet width is concerned. This may be because the 2D-PIV data is for planar orifice configuration, whereas 3D-PTV data is for the extended nozzle case. The vortex roll-up at the exit of the orifice is different in both cases. Hence, there is a difference in the jet spread. However, the velocity extents fairly match both the techniques, and the near jet discrepancies are due to the difference in the Reynolds number in the two cases.

Figure 4a compares ensemble-averaged non-dimensional streamwise and vertical velocities obtained from 2D-PIV and 3D-PTV along the centerline in the downstream direction. The velocities obtained from both techniques agree, but the 3D-PTV data shows early decay of the vortex ring at $X/D = 5$. The streamwise velocity obtained by 3D-PTV shows a few peaks as the vortex ring develops on its size and self-induced velocity due to statistically dependent data. During this period, the vortex ring entrains more ambient fluid and increases the mass flow rate. After reaching the maximum, the mass flow rate slowly decreases due to viscous dissipation of the ring and eventually reduces to zero far downstream. The centerline vertical velocity remains almost constant up to $X/D = 2.2$ and becomes slightly negative, then remains constant. The negative centerline velocity has a negligible magnitude to cause flow asymmetry. Figure 4b shows the ensemble-averaged non-dimensional streamwise and vertical velocity fluctuations in the downstream directions obtained from the
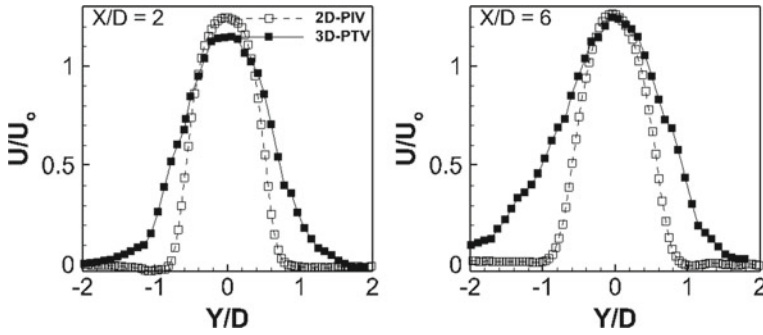
Fig. 3 Comparison of ensemble-averaged 2D-PIV ($L = 2.6$ and Re $= 470$) and 3D-PTV ($L = 2.73$ and Re $= 1075$) data of circular synthetic jet at two downstream locations

two measurement techniques. The velocity fluctuation is higher in the case of 3D-PTV may be because of the higher Reynolds number. The streamwise flow fluctuation reaches a peak at a similar streamwise location to the first peak of the streamwise centerline velocity due to the maximum entrainment of the surrounding fluid. The vertical flow fluctuation increases initially and remains nearly constant throughout the downstream location.

Figure 5 shows the non-dimensional velocity components in the *XY* plane at $Z/D = 0$ for (a) streamwise and (b) vertical velocities and (c) streamwise and (d) transverse velocities in the *XZ* plane at $Y/D = 0$. The corresponding non-dimensional standard deviation in the velocities is also shown in the figure for three streamwise locations $X/D = 2$, 4, and 6. The streamwise velocity and streamwise root mean square velocity is almost similar in both the *XY* and *XZ* planes, as seen in the figure. The maximum streamwise velocity remains the same along the streamwise direction, but the jet width increases streamwise. Whereas the streamwise root mean square velocity decreases along the streamwise direction. The results are in accordance with the literature showing mitigation of the normal and shear stresses along the
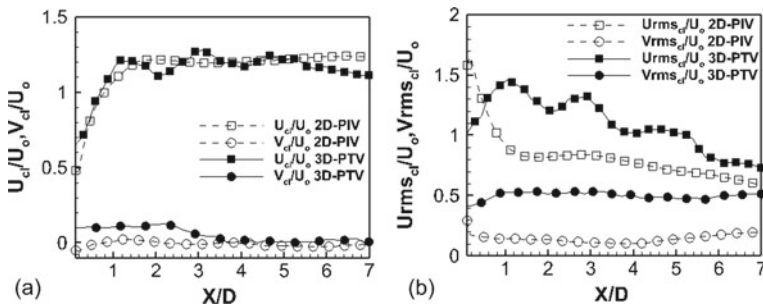

Fig. 4 Ensemble-averaged **a** non-dimensional streamwise and vertical velocity and **b** non-dimensional streamwise and vertical velocity fluctuations obtained along the centerline in *XY* plane at $Z/D = 0$

streamwise direction [12]. The transverse velocity (W) is more than the vertical velocity (V) in the near jet region. However, in the far jet region, both velocities are comparable. The transverse velocity fluctuation dominates the vertical velocity fluctuation, as noticed in the figure.

Figure 6 shows the ensemble-averaged non-dimensional vorticity magnitude distribution on three YZ planes at $X/D = 0.5$, 3.5, and 7. The spatial changes in the structure of the vortex ring can be seen in the figure. Near the orifice location ($X/D = 0.5$), the vortex ring starts developing by entraining the surrounding fluid. Hence, there is a non-uniformity in the plane. Whereas, at the mid-volume location or origin location ($X/D = 3.5$), the vortex ring gains its coherence showing the uniform vortex strength along the vortex core. At the exit of the measurement volume ($X/D = 7$), the vortex ring diffuses in the radial direction, and the surface of the ring shows dissipation, due to which the vortex ring loses its coherence.

3.2 Instantaneous Flow Structures

The instantaneous topology of a vortex ring is shown in Fig. 7 at $t/T = 0.225$, along with the three-dimensional velocity field. The isosurfaces of non-dimensional streamwise velocity (Fig. 7a) show that the jet is nearly axisymmetric. Figure 7b presents the isosurfaces of the normalized vorticity magnitude $\left(\frac{\omega}{\omega_{max}} = 0.4 \right)$, which defines the structure of the vortex ring. The cross section of the vortex is shown in Fig. 7c, with the streamwise velocity on the YZ plane located at $X/D = 3.1$. The figure also shows the trail of a vortex ring that just crossed the measurement volume. The vortex ring topology has also been presented using normalized Q-criterion $\left(\frac{Q}{Q_{max}} = 0.01 \right)$. The positive value of the criterion represents the vortex roll-up of the ring due to circulation filtering the shear effects.

Figure 8a–e shows the five consecutive instantaneous Z-vorticity fields in the XY plane at $Z/D = 0$. The areas of intense vorticity represent the location of the vortex ring. The vorticity of the ring is higher near the orifice, as seen in Fig. 8a, but as the vortex ring evolves, its vortex strength decreases downstream and remains limited to the ring core region, as seen in the far field of Fig. 8d. The possible reason for this is persisting vertical and transverse turbulence, as shown in Fig. 5, due to which the vortex ring loses its coherence. The complete cycle of the vortex ring evolution can be seen in the figure. It can also be noticed from the figures that the celerity of the vortex ring remains nearly the same as it advects downstream as the distance covered by the ring in the near orifice region is nearly the same as in the far stream region.

Figure 9 depicts the normalized vorticity magnitude isosurfaces (value 0.4) for the reconstructed flow structures of the circular synthetic jet shown in Fig. 9a–e. The vorticity field is normalized by the maximum value of the vorticity magnitude. One actuation cycle of a vortex ring evolution has been shown in Fig. 9a–e, where all the instantaneous reconstructions are 0.04 s ($t/T = 0.225$) apart. One cycle of the synthetic jet is nearly $T = 0.18$ s; hence, almost four instantaneous flow fields have
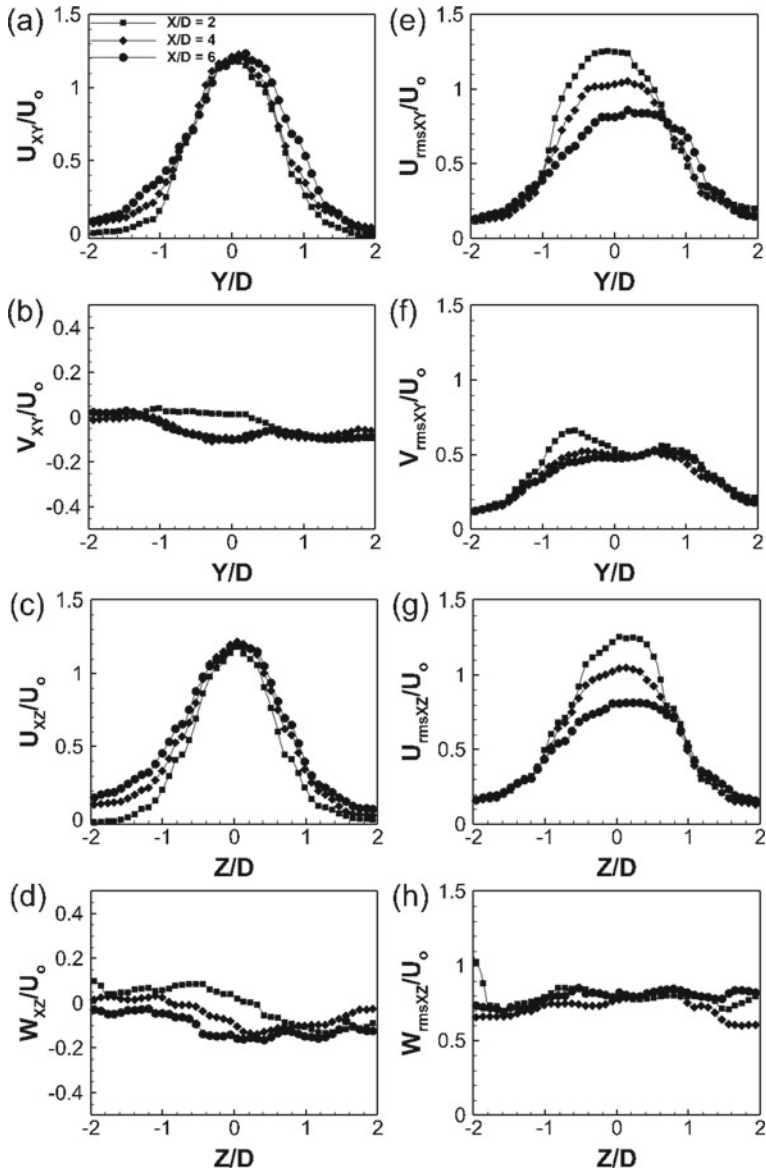
Fig. 5 Ensemble-averaged non-dimensional velocity component plots in the *XY* plane at *Z/D* = 0 for **a** streamwise and **b** vertical velocities and non-dimensional **c** streamwise and **d** transverse velocities in the *XZ* plane at *Y/D* = 0; along with the corresponding standard deviations of the velocity components at the three streamwise locations *X/D* = 2, 4, and 6
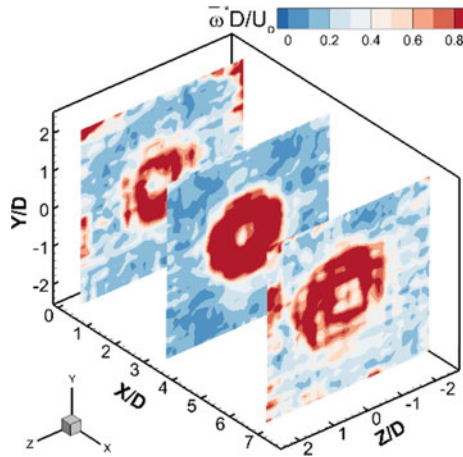
Fig. 6 Ensemble-averaged non-dimensional vorticity magnitude ($\overline{\omega}D/U_{o}$) distribution on three *YZ* planes at $X/D = 0.5, 3.5$, and 7
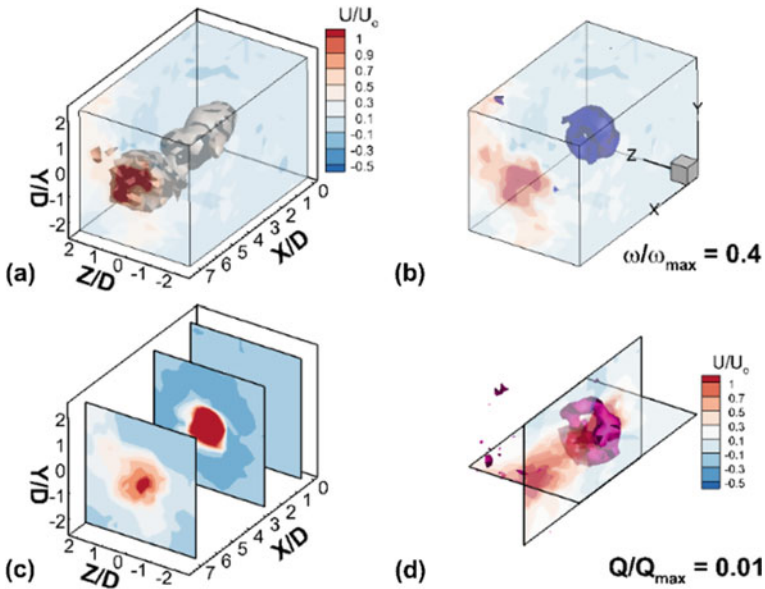
Fig. 7 Instantaneous vortex ring topology ($t/T = 0.225$) shown as **a** isosurfaces of non-dimensional streamwise velocity, **b** isosurface of normalized vorticity magnitude $\left(\frac{\omega}{\omega_{max}} = 0.4\right)$, **c** non-dimensional streamwise velocity at three different *YZ* planes, and **d** isosurfaces of normalized Q-criterion $\left(\frac{Q}{Q_{max}} = 0.01\right)$
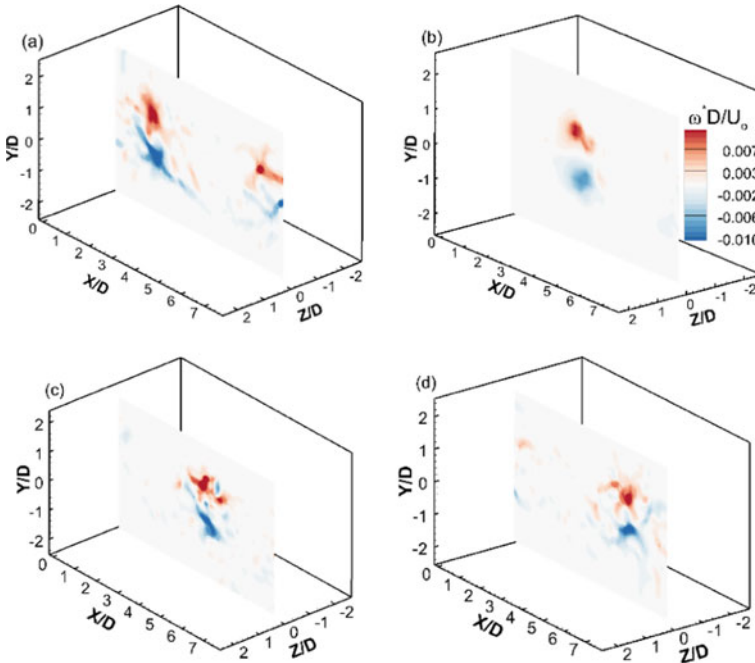
Fig. 8 Instantaneous non-dimensional spanwise vorticity ($\omega_z D/U_o$) for five consecutive fields for $L = 2.73$ and Re $= 1075$: **a** $t/T = 0$ s; **b** $t/T = 0.225$; **c** $t/T = 0.45$; **d** $t/T = 0.67$

been captured per cycle in this study. It can be seen from the figures that the vortex rings remain parallel to the nozzle plane. The vortex ring remains unchanged in the near jet region and loses coherence in the far jet region, as shown in Fig. 9d, e which owes to persisting vertical and transverse turbulence. The two successive vortex rings can also be seen in Fig. 9a, e. The distance between the two successive vortex rings is constant, which owes to the fixed formation number ($L = 2.73$). Figure 10a–c shows the evolution of the vortex ring with time for another actuation cycle. The vortex ring remains unchanged during the advection up to mid-measurement volume. The ejection of another vortex ring from the synthetic jet orifice and its evolution with time can also be seen in Fig. 10d, e.

4 Conclusions

The 3D-PTV experiment was carried out to investigate an axisymmetric synthetic jet flow for the formation number (L) $= 2.73$ and Re $= 1075$. The ensemble-averaged velocity line graphs followed the conventional velocity profiles of the circular synthetic jet. The similarities and differences in the velocity profiles obtained from the 3D-PTV and 2D-PIV measurement techniques have been presented for the
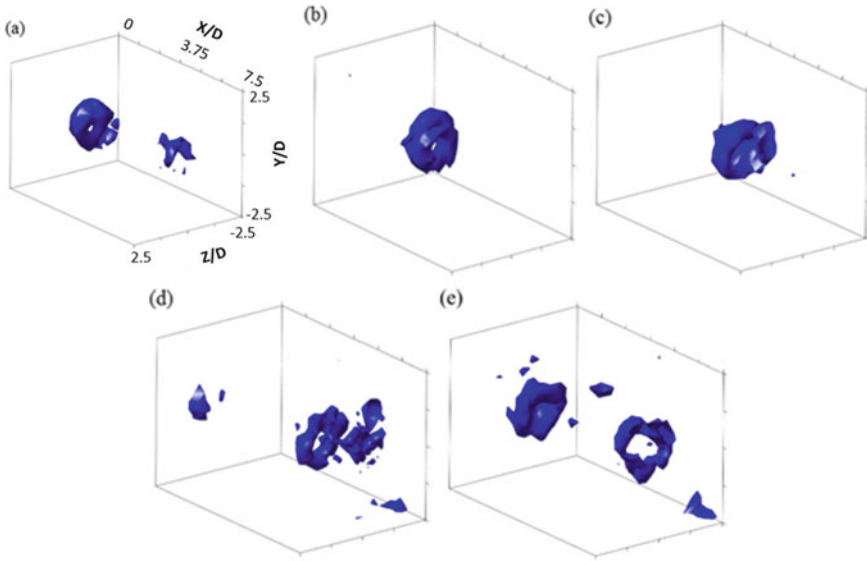
Fig. 9 Evolution of the circular synthetic jet vortex ring, illustrated by the isosurfaces of normalized vorticity magnitude ($\omega/\omega_{max} = 0.4$) for $L = 2.73$ and $Re = 1075$: **a** $t/T = 0$; **b** $t/T = 0.225$; **c** $t/T = 0.45$; **d** $t/T = 0.67$; **e** $t/T = 0.90$
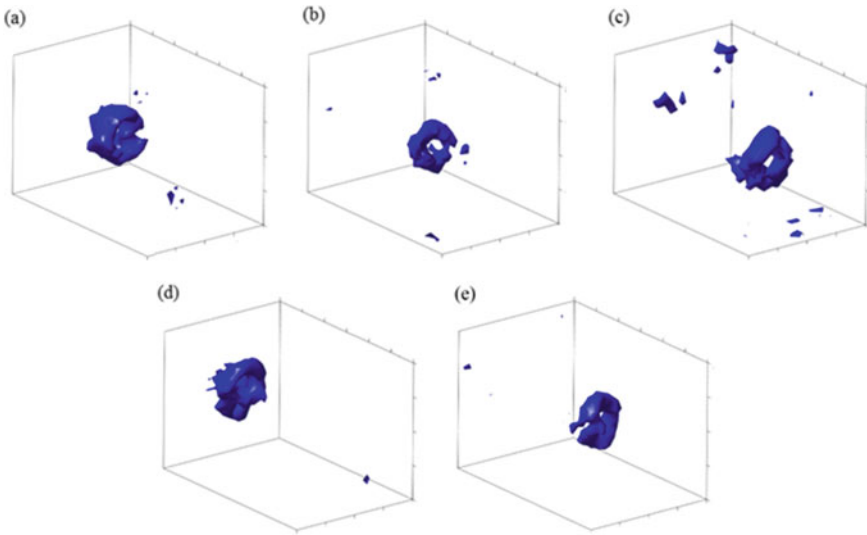

Fig. 10 Evolution of the circular synthetic jet vortex ring, illustrated by the isosurfaces of normalized vorticity magnitude ($\omega/\omega_{max} = 0.4$) for $L = 2.73$ and $Re = 1075$: **a** $t/T = 5.28$; **b** $t/T = 5.5$; **c** $t/T = 5.84$; **d** $t/T = 6.06$; **e** $t/T = 6.5$

same stroke length. The streamwise velocity showed similar magnitude and variations along the streamwise direction both in *XY* and *XZ* planes. The present study showed the importance of three-dimensional flow measurements as the magnitude of the transverse velocity (W) (which is generally ignored in the 2D flow measurements) was found to be more than that of the vertical velocity (V). The transverse root mean square velocity was also found to dominate the vertical root mean square velocity. The evolution of reconstructed instantaneous vortex rings with time was also shown in the study with the help of isosurfaces of normalized vorticity magnitude for two actuation cycles. The streamwise dissipation of the vortex rings was noticed in the far flow field, which owed to the persisting vertical and transverse turbulence along the downstream. The limitation of the study was the spatial resolution of the 3D vector field owing to the medium particle density of raw images.

References

1. Feng LH, Wang JJ (2014) Modification of a circular cylinder wake with synthetic jets: vortex shedding modes and mechanism. Eur J Mech B: Fluids 43:14–32
2. You D, Moin P (2008) Active control of flow separation over an airfoil using synthetic jets. J Fluids Struct 23:1349–1357
3. Smith DR (2002) Interaction of synthetic jet with crossflow boundary layer. AIAA J 40(11):2277–2288
4. Chaudhary M, Puranik B, Agarwal A (2010) Heat transfer characteristics of synthetic jet impingement cooling. Int J Heat Transf 53(5):1057–1069
5. Glezer A, Amitay M (2002) Synthetic jets. Annu Rev Fluid Mech 34:503
6. Glezer A (1988) The formation of vortex rings. Phys Fluids 31(12):3532–3542
7. Holman R, Utturkar Y, Mittal R, Smith BL, Cattafesta L (2005) Formation criteria for synthetic jets. AIAA J 43(10):2110–2116
8. Krishnan G, Mohseni K (2009) An experimental and analytical investigation of rectangular jets. J Fluids Eng 131:121101
9. Wang L, Feng LH, Wang JJ, Li T (2017) Parametric influence on the evolution of low-aspect-ratio rectangular synthetic jets. J Visualization 21:105
10. Jain M, Puranik B, Agarwal A (2011) A numerical investigation of effects of cavity and orifice parameters on the characteristics of a synthetic jet flow. Sens Actuators A 165:351–366
11. Panigrahi PK, Schroeder A, Kompenhans J (2008) Turbulent structures and budgets behind permeable ribs. Exp Therm Fluid Sci 32(4):1011–1033
12. Wang L, Feng LH, Wang JJ, Li T (2018) Characteristics and mechanism of mixing enhancement for noncircular synthetic jets at low Reynolds number. Exp Therm Fluid Sci 98:731–743
13. Shi XD, Feng LH, Wang JJ (2019) Evolution of elliptical synthetic jets at low Reynolds number. J Fluid Mech 868:66–96
14. Kähler CJ, Scharnowski S, Cierpka C (2012) On the uncertainty of Digital PIV and PTV near walls. Exp Fluids 52(6):1641–1656